Observed Signatures of the Barotropic and Baroclinic Annular Modes in Cloud Vertical Structure and Cloud Radiative Effects

YING LI AND DAVID W. J. THOMPSON

Department of Atmospheric Science, Colorado State University, Fort Collins, Colorado

(Manuscript received 28 September 2015, in final form 24 March 2016)

ABSTRACT

The signatures of large-scale annular variability on the vertical structure of clouds and cloud radiative effects are examined in vertically resolved *CloudSat* and other satellite and reanalysis data products. The northern and southern ''barotropic'' annular modes (the NAM and SAM) have a complex vertical structure. Both are associated with a meridional dipole in clouds between subpolar and middle latitudes, but the sign of the anomalies changes between upper, middle, and lower tropospheric levels. In contrast, the northern and southern baroclinic annular modes have a much simpler vertical structure. Both are linked to same-signed anomalies in clouds extending throughout the troposphere at middle to high latitudes. The changes in cloud incidence associated with both the barotropic and baroclinic annular modes are consistent with dynamical forcing by the attendant changes in static stability and/or vertical motion. The results also provide the first observational estimates of the vertically resolved atmospheric cloud radiative effects associated with hemispheric-scale extratropical variability. In general, the anomalies in atmospheric cloud radiative effects associated with the annular modes peak in the middle to upper troposphere, and are consistent with the anomalous trapping of longwave radiation by variations in upper tropospheric clouds. The southern baroclinic annular mode gives rise to periodic behavior in longwave cloud radiative effects at the top of the atmosphere averaged over Southern Hemisphere midlatitudes.

1. Introduction

The advent of remotely sensed observations of clouds and radiative fluxes has provided an unprecedented opportunity to examine the two-way linkages between climate variability and cloud structure. The purpose of this study is to exploit a range of such spaceborne observations to explore the signature of large-scale ''annular'' variability in the structure of clouds and cloud radiative effects at extratropical latitudes. A key aspect of the work is its emphasis on vertically resolved *CloudSat* data products.

Annular variability in the extratropical circulation can be viewed in the context of two ''classes'' of structures: barotropic and baroclinic annular modes. The barotropic annular structures correspond to the southern and northern annular modes (SAM and NAM) and are associated with north–south shifts of the extratropical eddy-driven jet (Hartmann and Lo 1998; Thompson and Wallace 2000; Limpasuvan and Hartmann 2000). The southern and northern baroclinic annular structures (SBAM and NBAM) correspond to the pulsation of eddy kinetic energy throughout much of the middle and high latitudes in each hemisphere and are associated with a periodicity on ~20–25-day time scale, particularly in the Southern Hemisphere (Thompson and Woodworth 2014; Thompson and Li 2015). The very different signatures of the baroclinic and barotropic annular modes suggest that they have very different signatures in cloud vertical structure.

The signature of the barotropic annular modes in clouds has been investigated in several recent studies [e.g., see the recent review by Ceppi and Hartmann (2015)]. Meridional shifts in the extratropical jet and storm track (which project onto the barotropic annular mode) have been linked to changes in free tropospheric clouds in both the Southern (Grise et al. 2013; Grise and Polvani 2014; Ceppi and Hartmann 2015) and Northern Hemisphere (Li et al. 2014a). They are also linked to robust changes in top of the atmosphere (TOA) longwave cloud radiative effects (Grise et al. 2013; Li et al.

Corresponding author address: Ying Li, Department of Atmospheric Science, Colorado State University, 3915 W. Laporte Ave., Fort Collins, CO 80521.
E-mail: yingli@atmos.colostate.edu

DOI: 10.1175/JCLI-D-15-0692.1

2014a; Ceppi and Hartmann 2015), consistent with the response of mid- to high-level clouds to anomalous vertical motion (Li et al. 2014b). The relationships between jet latitude and TOA shortwave cloud radiative effects appear to be relatively weak due to the canceling contributions from high and low clouds (Grise et al. 2013). They are also highly model dependent (Grise and Polvani 2014; Ceppi and Hartmann 2015).

Many key questions regarding the signatures of large-scale extratropical variability in clouds and radiative effects remain to be addressed. Previous studies on the linkages between the barotropic annular modes and clouds have focused primarily on numerical output (e.g., Ceppi et al. 2014; Grise and Polvani 2014; Ceppi and Hartmann 2016) and/or cloud data from the International Satellite Cloud Climatology Project (ISCCP) and radiative fluxes derived from the Clouds and the Earth's Radiant Energy System (CERES; e.g., Grise et al. 2013; Grise and Polvani 2014). The ISCCP and CERES observations are invaluable data sources but provide limited information about the vertical structure of cloud incidence and radiative effects. The signature of the SAM on clouds and cloud radiative effects has not been characterized in vertically resolved *CloudSat* observations. As far as we know, the signatures of baroclinic annular variability in clouds or cloud radiative effects have yet to be explored in observations or numerical models.

The objective of this study is to analyze and diagnose the observed influence of the large-scale annular variability on the vertical structure of clouds and cloud radiative effects in both hemispheres. The satellite and reanalysis data are described in section 2, results are presented in section 3, and implications for climate variability are discussed in section 4.

2. Data and methods

a. Data

1) *CloudSat* cloud incidence

Cloud fraction data are obtained from the combined *CloudSat* Cloud Profiling Radar (CPR) and *CALIPSO* lidar retrievals 2B-GEOPROF-lidar product (version P2R04; Mace et al. 2009) and are presented as "cloud incidence." Cloud incidence provides a quantitative estimate of the likelihood of a cloud within a given atmospheric volume and is calculated as per our previous work (Li et al. 2014a,b). The CPR aboard *CloudSat* is a 94-GHz nadir-pointing radar. It provides radar reflectivity profiles at a vertical resolution of 240 m, with a 1.4-km cross track and 2.5-km along track footprint, up to 82° latitude. The near-nadir-pointing CPR has limitations on spatial sampling on daily time scales. For this reason, the cloud incidence data are binned into 5-day mean with spatial resolution of 2.5° (latitude) × 2.5° (longitude) × 240 m (vertical), and are analyzed over the period 2007–10.

The limitations of the *CloudSat* and *CALIPSO* measurements are discussed in detail in our previous work (e.g., section 2a in Li et al. 2014b). The most serious limitations of the combined *CloudSat* and *CALIPSO* data lie in detecting 1) near-surface clouds due to ground clutter and 2) low-level nonprecipitating water clouds beneath high optically thick clouds for which the lidar pulse is fully attenuated and water droplets are too small to be detected by the radar (e.g., Mace et al. 2009). Despite these limitations, the combination of the active remote sensors of the *CloudSat* radar and *CALIPSO* lidar sample the majority of the hydrometeor layers within Earth's atmosphere.

2) *CloudSat* cloud radiative heating rates

Cloud radiative heating rates are derived from the combined *CloudSat–CALIPSO* 2B-FLXHR-lidar product (version P2R04), which utilizes the combined *CloudSat–CALIPSO* cloud observations and lidar-based aerosol retrievals (Henderson et al. 2013). The product provides profiles of estimates of the 1) upward and downward longwave radiative fluxes, 2) upward and downward shortwave radiative fluxes, and 3) all-sky radiative heating rates at 240-m vertical increments.

3) *CloudSat* ECMWF-AUX product

The *CloudSat*–European Centre for Medium-Range Weather Forecasts auxiliary product (ECMWF-AUX) provides ECMWF state variable data interpolated onto the same spatial and temporal resolution as the *CloudSat* track. The ECMWF-AUX product is used to derive clear-sky radiative heating rates.

4) CERES cloud radiative effects

Cloud radiative effects are derived from CERES SYN1deg product version 3A, available on 1.0° × 1.0° grid resolution and from March 2000 to November 2014 (Loeb et al. 2009; Kato et al. 2013).

5) AIRS cloud radiative effects

Outgoing longwave radiation fluxes are also derived from the Atmospheric Infrared Sounder (AIRS) version-6 daily mean level-3 gridded products (Aumann et al. 2003; Chahine et al. 2006; available at ftp://acdisc.gsfc.nasa.gov/ftp/data/s4pa/Aqua_AIRS_Level3/AIRX3STD.006/). They are available on 1.0° × 1.0° grid resolution, and from September 2002 to present.

6) ERA-INTERIM

We also use 4 times daily output from the EMMWF interim reanalysis (ERA-Interim; Simmons et al. 2007; Dee et al. 2011). The reanalysis is analyzed on a 1.5° × 1.5° horizontal mesh and at 37 pressure levels from 1979 to 2011.

b. Methods

The annular mode indices used here are generated as per Thompson and Woodworth (2014) and Thompson and Li (2015). Briefly, the SAM and NAM indices are defined as the leading principal component (PC) time series of the anomalous daily-mean zonal-mean zonal wind $[u]$ over all levels and latitudes within the domain 1000–200 hPa and 20°–70°S/N. The SBAM and NBAM indices are defined as the leading PC time series of the anomalous daily-mean zonal-mean eddy kinetic energy (EKE) over the same domain, where EKE is defined as $0.5[u^{*2} + v^{*2}]$. Here, brackets denote zonal-mean quantities and the asterisks (*) indicate departures from the zonal mean. Eddy kinetic energy is calculated at four times daily time scales before computing daily averages. Note that for the NBAM index, the eddy kinetic energy is calculated only for zonal wavenumbers 4 and higher to minimize the effects of stationary waves in the time series (see Thompson and Li 2015). In all cases, the data are weighted by the square root of the cosine of latitude and the mass represented by each vertical level in the ERA-Interim before calculating the PC time series.

Power spectra for time series based on AIRS and CERES are found by 1) calculating power spectra for subsets of the time series that are 250 days in length with a 125-day overlap between adjacent subsets (split-cosine-bell tapering is applied to 5% of the data on each end of the subset time series), 2) averaging the power spectra over all subsets of the time series, and 3) applying a three-point running mean to the resulting mean power spectrum.

The static stability (N^2) is defined as $(g/\theta)(\partial\theta/\partial z)$, where g is 9.81 m s^{-2} and θ is potential temperature, and tropopause height is identified using the World Meteorological Organization lapse rate definition.

The cloud radiative heating rates at a given atmospheric level are defined as the all-sky minus clear-sky radiative heating rates. All-sky radiative heating rates are obtained from the *CloudSat* 2B-FLXHR-lidar product. Clear-sky radiative heating rates within an atmospheric level are calculated as follows:

$$\frac{dT}{dt} = \frac{g}{C_p}\frac{dF_{\text{net}}}{dp}, \tag{1}$$

where dT/dt is time rate of change of temperature, $F_{\text{net}} = F^{\uparrow} - F^{\downarrow}$ is the net flux passing through the layer derived from the *CloudSat* 2B-FLXHR-lidar product, g is the gravitational constant, C_p is the specific heat capacity of dry air, and p is pressure obtained from the *CloudSat* ECMWF-AUX product.

The shortwave fluxes for each cloud profile have been normalized, following Haynes et al. (2013), using the averaged incoming shortwave radiation at the latitude and day of each profile observations. Thus the normalized shortwave fluxes accounted for the diurnal cycle in solar insolation. The shortwave cloud radiative heating is then calculated by applying Eq. (1) to the normalized shortwave fluxes.

3. Results

a. Dynamical context

Before we examine the signatures of the annular modes in clouds and cloud radiative heating, we briefly review their signatures in dynamical fields that are relevant for cloud development.

The top panels in Figs. 1 and 2 show different daily-mean, zonal-mean dynamical fields regressed onto daily-mean values of the NAM and SAM indices. Note that the regressions are based on year-round data and thus the wind and temperature anomalies have weaker amplitude in the stratosphere than those derived from results based on the active seasons for stratosphere–troposphere coupling [e.g., winter in the Northern Hemisphere (NH); spring in the Southern Hemisphere (SH)].

The anomalies associated with the NAM are generally shifted ~5°–10° equatorward of their SAM counterparts, but otherwise both patterns exhibit a high degree of hemispheric symmetry. As noted extensively in previous work (e.g., Hartmann and Lo 1998; Thompson and Wallace 2000; Limpasuvan and Hartmann 2000), the positive polarities of the barotropic annular modes are characterized by the following attributes:

- A meridional dipole in the zonal-mean zonal wind with primary centers of action located ~35°–40° and ~55°–60° latitude (Figs. 1a,b, shading).
- Paired meridional overturning cells with rising motion at subpolar and tropical latitudes juxtaposed against sinking motion at midlatitudes (Figs. 1a,b, contours).
- Positive temperature anomalies in the midlatitude troposphere and negative temperature anomalies in the high latitude troposphere, and negative temperature anomalies in the polar stratosphere (Figs. 2a,b, shading).
- Increases in static stability in the upper troposphere ~60°–70° and at the surface ~40°–60°, but decreases in static stability in the upper troposphere ~40°–60° and at

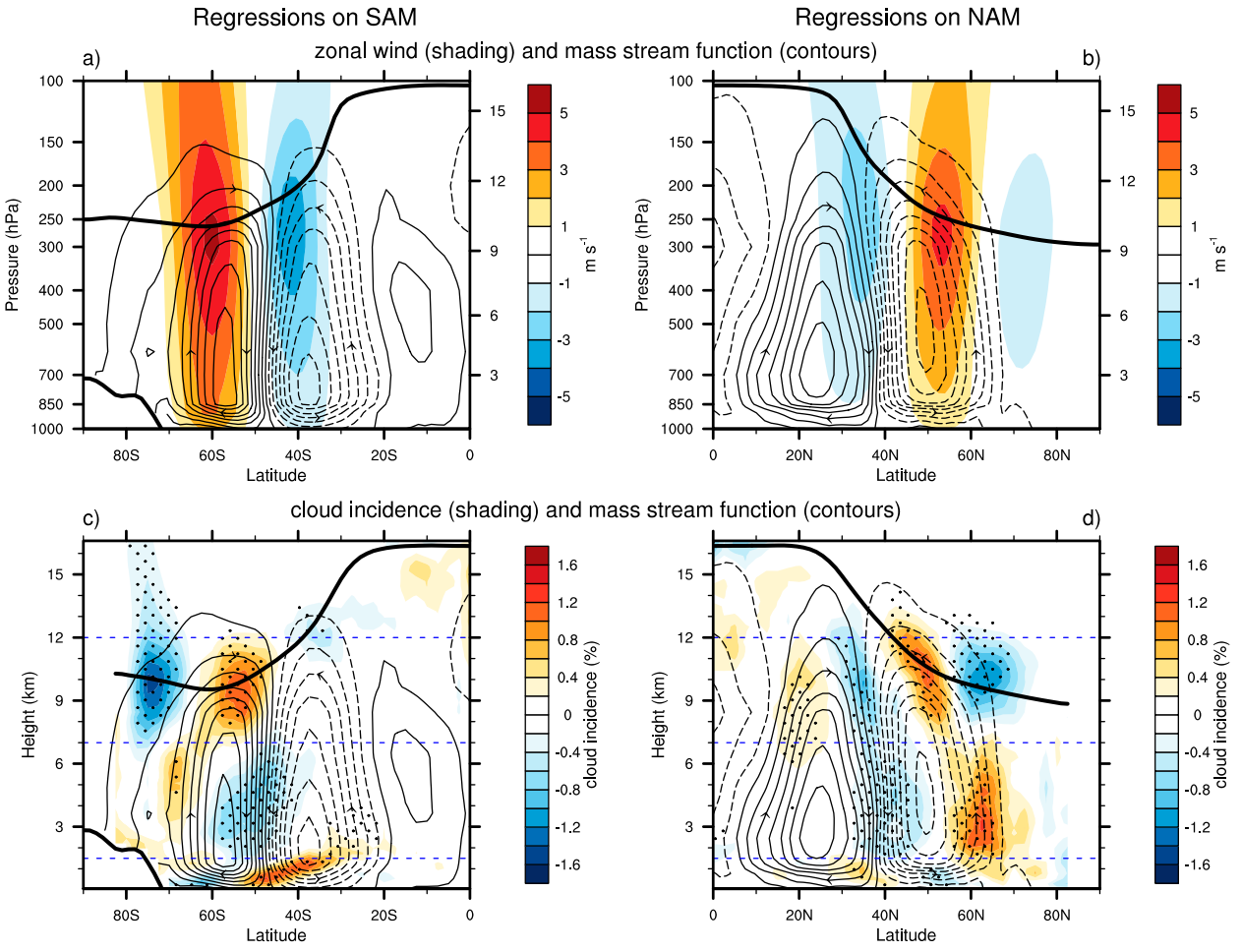

FIG. 1. (top) Regressions of daily-mean, zonal-mean zonal wind (shading) and mass streamfunction (contours) anomalies onto standardized daily-mean values of the (left) SAM and (right) NAM indices. (bottom) Regressions of pentad-mean, zonal-mean cloud incidence (shading) anomalies onto standardized pentad-mean values of the (left) SAM and (right) NAM indices. The contours in the bottom panels are reproduced from the top panels. The thick black line indicates the height of the climatological-mean tropopause and zonally averaged surface elevation over Antarctica. Black stippling indicates results that exceed the 95% confidence level based on a two-tailed test of the t statistic, with the effective degrees of freedom computed as per Bretherton et al. [1999, their Eq. (31) therein]. Horizontal dashed blue lines are drawn at 12, 7, and 1.5 km. Cloud incidence is derived from *CloudSat* product for the period January 2007 to December 2010. All other fields are derived from the ERA-Interim reanalysis for the period January 1979 to December 2011. The mass streamfunction anomalies are at $-0.5, 0.5, 1.5 \times 10^9\,\mathrm{kg\,s^{-1}}$, etc.

the surface ~60°–70° (Figs. 2a,b, contours). The changes in static stability associated with the NAM and SAM follow from the changes in temperature, but to our knowledge have not been documented in previous work.

The top panels in Figs. 3 and 4 review the dynamical signatures of the baroclinic annular modes. As also noted in previous work (e.g., Thompson and Woodworth 2014; Thompson and Li 2015), the baroclinic annular modes have large amplitude in eddy kinetic energy, but weak amplitude in the zonal-mean temperature and wind fields relative to the barotropic annular modes. The positive polarities of the SBAM and NBAM are characterized by the following:

- Broad monopoles in eddy kinetic energy that span much of the extratropics (Figs. 3a,b, shading).
- Meridional overturning cells with rising motion at subpolar and tropical latitudes juxtaposed against sinking motion centered ~30°–40° latitude (Figs. 3a,b, contours).
- Positive temperature anomalies in the extratropical troposphere poleward of ~50° (Figs. 4a,b, shading). Note that the positive temperature anomalies coincide with rising motion. Hence, the vertical motion anomalies associated with the baroclinic annular modes may be viewed as thermally driven, rather than thermally damped, as is the case for the barotropic annular modes (Thompson and Woodworth 2014; Thompson and Li 2015).

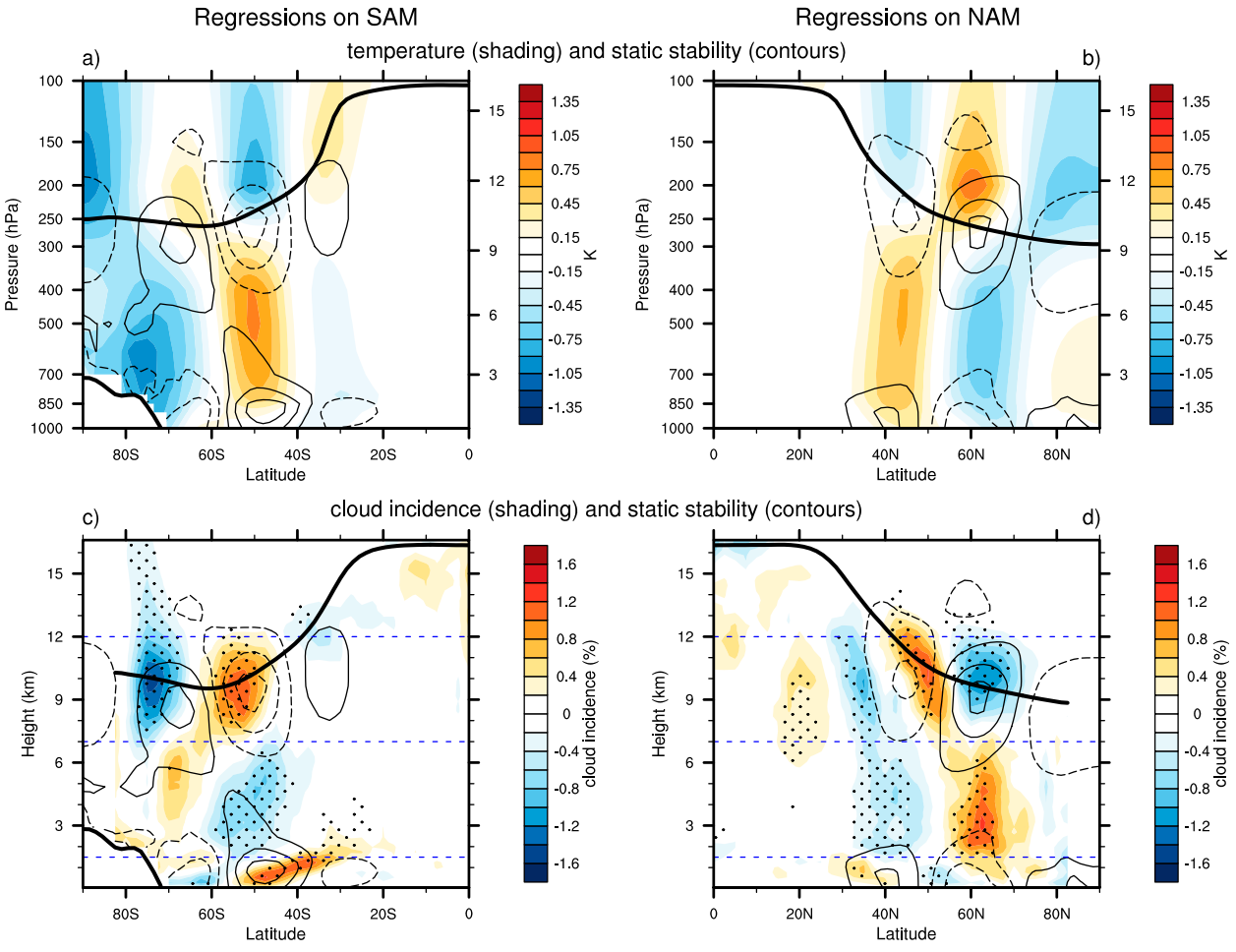

FIG. 2. (top) Regressions of daily-mean, zonal-mean temperature (shading) and static stability anomalies (contours) onto standardized daily-mean values of the (left) SAM and (right) NAM indices. (bottom) The cloud incidence anomalies (shading) are reproduced from the bottom panels of Fig. 1, and the static stability anomalies (contours) are reproduced from the top panels. The thick black line indicates the height of the climatological-mean tropopause and zonally averaged surface elevation over Antarctica. Black stippling indicates results that exceed the 95% confidence level based on a two-tailed test of the t statistic, with the effective degrees of freedom computed as per Bretherton et al. [1999, their Eq. (31)]. Horizontal dashed blue lines are drawn at 12, 7, and 1.5 km. The static stability anomalies are at -3, 3, 9×10^{-4} s^{-2}, etc.

- Decreases in static stability in the upper troposphere near ~60° and increases at the surface near ~60° (Figs. 4a,b, contours). As is the case with the barotropic annular modes, the changes in static stability associated with the SBAM and NBAM follow from changes in temperature.

b. *Spatial signatures of the annular modes in zonally averaged cloud vertical structure*

The bottom panels in Figs. 1 and 2 indicate the associated signatures of the SAM and NAM in zonal-mean cloud incidence (note that the cloud incidence anomalies are reproduced in the bottom panels of Figs. 1 and 2 so that they can be compared with anomalies in both the mass streamfunction and static stability). The bottom panels in Figs. 3 and 4 show analogous results for the SBAM and NBAM. All cloud incidence results are based on the *CloudSat*/*CALIPSO* product for the 2007–10 period (see section 2a). In contrast to the dynamical fields reviewed above, the cloud incidence regressions are based on standardized pentad-mean data. Results based on cloud fraction from ERA-Interim for both the 2007–10 and 1979–2011 periods are shown in the appendix (Fig. A1).

We focus here on the signatures of the annular modes in the zonal-mean circulation. Results for the zonally varying circulation are presented in the appendix (Fig. B1) for reference. We focus on the zonal mean for two reasons: 1) Regressions based on pentad-mean *CloudSat* are less susceptible to nadir sampling variability effects when the data are averaged along latitude circles than they are at a single grid box (i.e., more swaths are included in the 5-day averages in the zonal

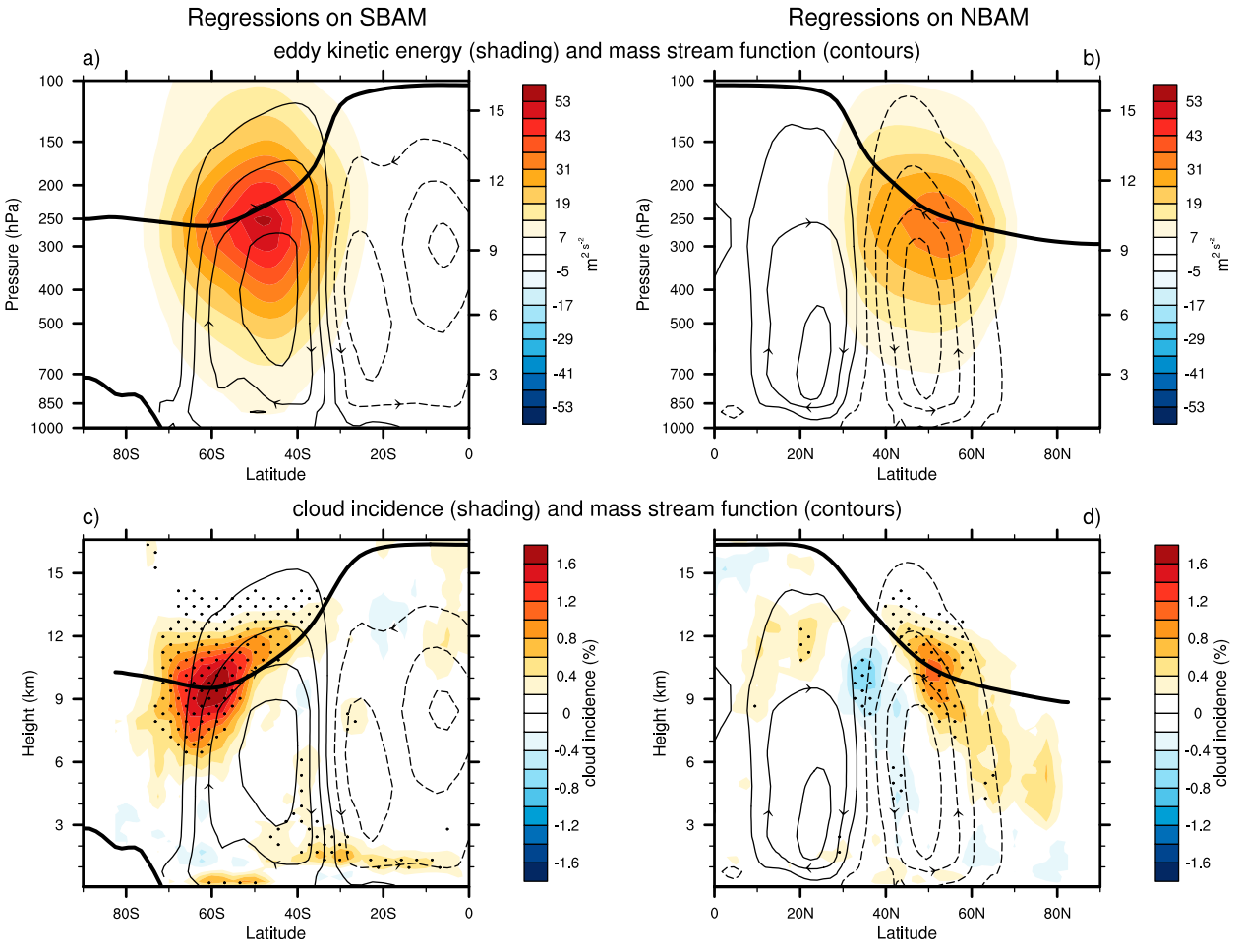

FIG. 3. (top) Regressions of daily-mean, zonal-mean eddy kinetic energy (shading) and mass streamfunction (contours) anomalies onto standardized daily-mean values of the (left) SBAM and (right) NBAM indices. (bottom) Regressions of pentad-mean, zonal-mean cloud incidence (shading) anomalies onto standardized pentad-mean values of the (left) SBAM and (right) NBAM indices. The contours in the bottom panels are reproduced from the top panels. The thick black line indicates the height of the climatological-mean tropopause and zonally averaged surface elevation over Antarctica. Black stippling indicates results that exceed the 95% confidence level based on a two-tailed test of the t statistic, with the effective degrees of freedom computed as per Bretherton et al. [1999, their Eq. (31)]. The mass streamfunction anomalies are at $-0.5, 0.5, 1.5 \times 10^9\,\mathrm{kg\,s^{-1}}$, etc.

mean than at a single grid box). Also, 2) the signatures of the annular modes in cloud incidence along latitude circles have a strong zonally symmetric component, consistent with their dynamical signatures (Fig. B1). The most pronounced zonal asymmetries are found in the NH where (as expected) the cloud incidence anomalies associated with the NAM have largest amplitude over the North Atlantic sector (Fig. B1b).

In general, the zonal-mean cloud incidence anomalies associated with the annular modes are consistent with the physical linkages between extratropical dynamics and cloud incidence, as documented in *CloudSat* data in our previous work (Li et al. 2014b). As discussed below, the anomalies in cloud incidence near the tropopause are consistent with the changes in near-tropopause static stability; the anomalies in cloud incidence in the middle and upper troposphere are consistent with the changes in large-scale vertical motion and the amplitudes of baroclinic waves; and the anomalies in lower tropospheric cloud incidence are consistent with the changes in near-surface static stability.

We begin our discussion with the SAM.

1) SAM

As noted in the introduction, Grise et al. (2013; see Fig. 3 therein) also examine the observed signature of the SAM in cloud incidence, but in passive ISCCP measurements with poor vertical resolution rather than active *CloudSat* measurements with high vertical

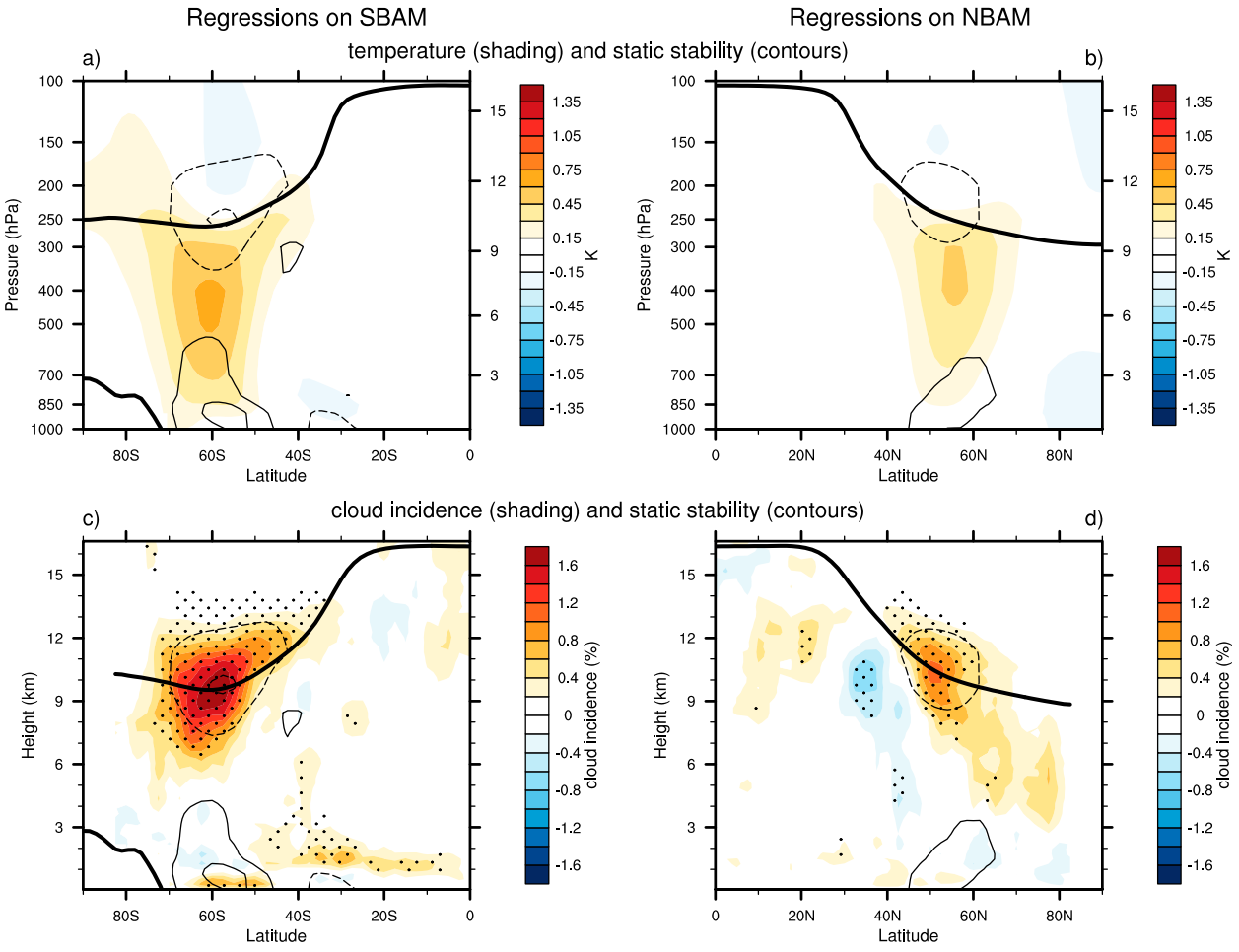

FIG. 4. (top) Regressions of daily-mean, zonal-mean temperature (shading) and static stability (contours) anomalies onto standardized daily-mean values of the (left) SBAM and (right) NBAM indices. (bottom) The cloud incidence anomalies (shading) are reproduced from the bottom panels of Fig. 3, and the static stability anomalies (contours) are reproduced from the top panels. The thick black line indicates the height of the climatological-mean tropopause and zonally averaged surface elevation over Antarctica. Black stippling indicates results that exceed the 95% confidence level based on a two-tailed test of the t statistic, with the effective degrees of freedom computed as per Bretherton et al. [1999, their Eq. (31)]. The static stability anomalies are at $-3, 3, 9 \times 10^{-4}\,\mathrm{s}^{-2}$, etc.

resolution. We will compare our results with those derived from ISCCP data where warranted.

The vertical structure of cloud incidence associated with the SAM (Fig. 1c) can be viewed in the context of three distinct height regimes, as delineated by the light dashed horizontal lines in the bottom panels of Figs. 1 and 2: 1) upper troposphere/lower stratospheric clouds, 2) middle tropospheric clouds, and 3) lower tropospheric clouds.

(i) Upper troposphere/lower stratosphere (~7–12 km)

At upper tropospheric levels, the positive polarity of the SAM is marked by two primary centers of action: positive cloud incidence anomalies at ~50°S and negative cloud incidence anomalies at ~70°S that extend into the lower polar stratosphere. The changes in clouds at this vertical level are not clearly mirrored in the changes in large-scale vertical motion (Fig. 1c). However, they are consistent with the attendant changes in upper tropospheric stability (Fig. 2c). The region of anomalously positive cloud incidence near ~50°S is closely collocated with a region of anomalously low static stability; the region of anomalously low cloud incidence ~70°S is closely collocated with anomalously high static stability.

As far as we know, the meridional dipole in upper tropospheric cloud incidence associated with the SAM has not been noted in previous work. It is reproducible in daily-mean ERA-Interim output (Fig. A1). But it is not apparent in the ISCCP-based results shown in Grise et al. (2013, cf. their Fig. 3). The differences between the signatures of the SAM in upper tropospheric clouds shown here and in Grise et al. (2013) may derive from differences in analysis technique. However, we have

checked our results in data for the December–February season [as used in Grise et al. (2013)], and the dipole is largely unchanged. The absence of a dipole in ISCCP-based results may also derive from categorization errors in the ISCCP data. For example, passive instruments (such as those used in ISCCP) frequently mistake thin, high clouds as midlevel clouds in regions of pronounced boundary layer cloudiness (Mace et al. 2011). Additionally, the ISCCP categorization marks clouds as upper-level if cloud-top pressure is less than 440 hPa (i.e., above 6.5 km), such that midtropospheric clouds with cloud top less than 440 hPa may be erroneously categorized as upper-level clouds. A detailed comparison of results based on ISCCP and *CloudSat* is beyond the scope of this study.

(ii) Middle troposphere (~1.5–7 km)

In the middle troposphere, the positive polarity of the SAM is marked by reduced cloud incidence centered ~50°S, consistent with the anomalous downward motion there (Fig. 1c). It is also marked by weak increases in clouds near ~70°S consistent with anomalous rising motion in the high-latitude troposphere. The cloud incidence anomalies centered at ~50°S are robust in both *CloudSat* (Fig. 1c) and ERA-Interim (Fig. A1). The cloud incidence anomalies near ~70°S are only weakly apparent in the *CloudSat* results (Fig. 1c) but are much more clear in results based on ERA-Interim during both the *CloudSat* era and the longer record of 1979–2011 (Fig. A1, top row). There are two possible reasons for the relatively weak amplitude of high-latitude cloud anomalies based on the *CloudSat* data relative to those derived from the ERA-Interim reanalysis: 1) the *CloudSat* data have limited spatial sampling and thus may undersample the covariability between the SAM and clouds in certain locations, and 2) the variance of cloud incidence anomalies may be biased in ERA-Interim relative to *CloudSat* observations.

The middle tropospheric cloud anomalies shown in (Fig. 1c) are reminiscent not of the signature of the SAM in *middle* tropospheric clouds derived from ISCCP, but of the signature of the SAM in *upper* tropospheric clouds derived from ISCCP (Grise et al. 2013). We believe the differences between results based on *CloudSat* and ISCCP likely derive from the passive ISCCP measurements conflating clouds at different levels, as discussed earlier.

(iii) Lowermost troposphere (0–1.5 km)

Near the surface, the positive polarity of the SAM is associated with positive cloud incidence anomalies ~45°S and negative cloud incidence anomalies ~65°S. The changes in near-surface clouds are consistent with the changes in near-surface static stability (Fig. 2c). Note that the regions of free tropospheric descending motion near ~45°S are associated with decreases in clouds in the free troposphere (as discussed above) but increases in clouds in the boundary layer (see also Klein and Hartmann 1993). Likewise, regions of free tropospheric ascending motion poleward of 65°S are associated with increases in clouds in the free troposphere but decreases in the boundary layer. A similar out-of-phase relationship between clouds at the surface and in the middle troposphere is evident when extratropical cloud incidence is plotted as a function of free tropospheric vertical motion (Li et al. 2014b; cf. their Fig. 5).

The meridional dipole in near-surface clouds associated with the SAM is evident in both ERA-Interim (Figs. A1b,c) and also in the ISCCP-based results shown in Fig. 3 of Grise et al. (2013). It is a very robust feature of the SAM in clouds. It is noteworthy that the amplitudes of cloud anomalies based on the *CloudSat* data are relatively weaker as compared to those derived from the ERA reanalysis at the surface and low levels, which could be due to limitations of the satellite retrievals as discussed in section 2a.

2) NAM

The vertical structure of cloud incidence associated with the NAM was explored in Li et al. (2014a) but is reproduced here for three reasons: 1) to facilitate comparison between cloud incidence anomalies associated with the NAM with those associated with other forms of extratropical variability, 2) to provide context for the analyses of cloud radiative heating rates shown in the next section, and 3) to exploit the larger sample size afforded by year-round pentad-mean data [the results in Li et al. (2014a) are based on monthly-mean wintertime data].

The signature of the NAM in cloud incidence (Figs. 1d and 2d) is very similar to that associated with the SAM but for two notable differences: 1) The cloud incidence (and corresponding circulation) anomalies associated with the NAM are shifted ~5°–10° equatorward of their SH counterparts, and 2) the signature of the NAM in near-surface clouds is much weaker than that associated with the SAM. As is the case for the SAM, the cloud incidence anomalies associated with the NAM are consistent with the underlying circulation anomalies. The NAM is associated with 1) a meridional dipole in upper tropospheric cloud incidence that mirrors the changes in upper tropospheric static stability (Fig. 2d) and 2) a similar but opposite signed dipole in the middle troposphere consistent with the changes in free tropospheric vertical motion (Fig. 1d). The primary features associated with the NAM are reproducible in results based on ERA-Interim (Figs. A1e,f).

Interestingly, the cloud incidence anomalies in Figs. 1d and 2d reveal a meridional tripole in upper tropospheric clouds that is not apparent in our previous analyses of the NAM (Li et al. 2014a). We have investigated the reasons for the differences in near-tropopause cloud incidence between this study and Li et al. (2014a), and they can be traced to three differences in analysis technique (see Fig. C1): 1) the results in Li et al. (2014a) are based on monthly-mean rather than pentad-mean cloud data, 2) the results in Li et al. (2014a) are based on data limited to the winter season whereas those shown here are based on data for all calendar months, and 3) the regressions in Li et al. (2014a) are based on a NAM index derived from PC analysis of height at 1000 hPa rather than the zonal-mean zonal wind at all tropospheric levels from 1000 to 200 hPa (PCs of the tropospheric zonal wind will tend to have slightly larger amplitude in the free troposphere). Hence, in contrast to Li et al. (2014a), the results shown here 1) are based on a larger sample size, 2) include submonthly variations in cloud incidence, 3) include summertime variations in cloud incidence, and 4) are based on a NAM index that has larger amplitude in the free tropospheric. We view the meridional tripole in upper tropospheric cloud incidence anomalies shown in Figs. 1d and 2d as a robust signature of the NAM.

3) SBAM AND NBAM

The signatures of the baroclinic annular modes in cloud incidence are very different than those associated with the SAM and NAM (bottom panels of Figs. 3 and 4). By far, the most prominent feature in cloud incidence associated with the SBAM and NBAM is widespread increases in cloud incidence extending throughout the troposphere at middle to high latitudes during periods of anomalously high eddy kinetic energy (i.e., the high index polarities of the SBAM and NBAM). The increases in midlevel cloud incidence have larger amplitude in the SH, and are consistent with both anomalous upward motion (Figs. 3c and 3d) and anomalously low static stability in the upper troposphere (Figs. 4c and 4d). They are also consistent with the relationships between cloud incidence and storm amplitude, as documented in Li et al. (2014b, cf. their Fig. 7).

The baroclinic annular modes are also associated with weak negative anomalies in cloud incidence ~35° in the upper troposphere in the vicinity of anomalous descending motion, particularly in the NH. In the case of the NBAM, the negative anomalies are evident in both *CloudSat* and ERA-Interim (Fig. 3c; see also Fig. A1, bottom row); in the case of the SBAM, they are only apparent in ERA-Interim (Fig. A1, penultimate row). The relatively weak amplitudes of the negative anomalies derive in part from the relatively weak variance in cloud incidence in the subtropical free troposphere (not shown).

The increases in near-surface clouds ~60°S (Figs. 3c and 4c) are robust in ERA-Interim and overlie increases in near-surface static stability. However, a similar feature is not found in association with the NBAM.

c. *Associated changes in cloud radiative effects*

1) ATMOSPHERIC CLOUD RADIATIVE EFFECTS

Figures 5 and 6 show pentad-mean longwave and shortwave atmospheric cloud radiative effects (ACRE) derived from *CloudSat* 2B-FLXHR-lidar product (see section 2) regressed onto the SAM and NAM (top panels) and SBAM and NBAM (bottom panels) indices. To our knowledge, the results provide the first observational estimate of the vertical profiles of atmospheric cloud radiative heating rates associated with annular variability.

The anomalies in longwave ACRE associated with the annular modes (Fig. 5) are generally consistent with the 1) trapping of outgoing longwave radiation by anomalies in upper level clouds and 2) emission of longwave radiation from the atmosphere to the surface by anomalies in lower-level clouds. In the upper troposphere, regions of anomalously positive cloud incidence are associated with anomalously positive longwave ACRE, and vice versa. In contrast, in the lower troposphere, regions of anomalously positive cloud incidence are associated with anomalously negative longwave ACRE, and vice versa. For example, in the upper troposphere, the SAM and NAM are associated with anomalously positive longwave ACRE at middle latitudes (Fig. 5, top panels) where cloud incidence is anomalously high (Fig. 1 bottom panels). Likewise, they are associated with anomalously negative longwave ACRE in the high-latitude troposphere where cloud incidence is anomalously low. The baroclinic annular modes are dominated by monopoles in positive longwave ACRE throughout the middle-upper troposphere between ~50° and 70°, particularly in the Southern Hemisphere. In the lower troposphere, the SAM is associated with anomalously negative longwave ACRE at ~40°S (Fig. 5a) where cloud incidence is anomalously high (Fig. 1c). Likewise, it is associated with anomalously positive longwave ACRE at ~60°S where cloud incidence is anomalously low.

The anomalies in shortwave ACRE (Fig. 6) are generally consistent with the absorption of shortwave radiation by cloud incidence anomalies. For examples: in the middle troposphere, the SAM and NAM are associated with anomalously negative shortwave

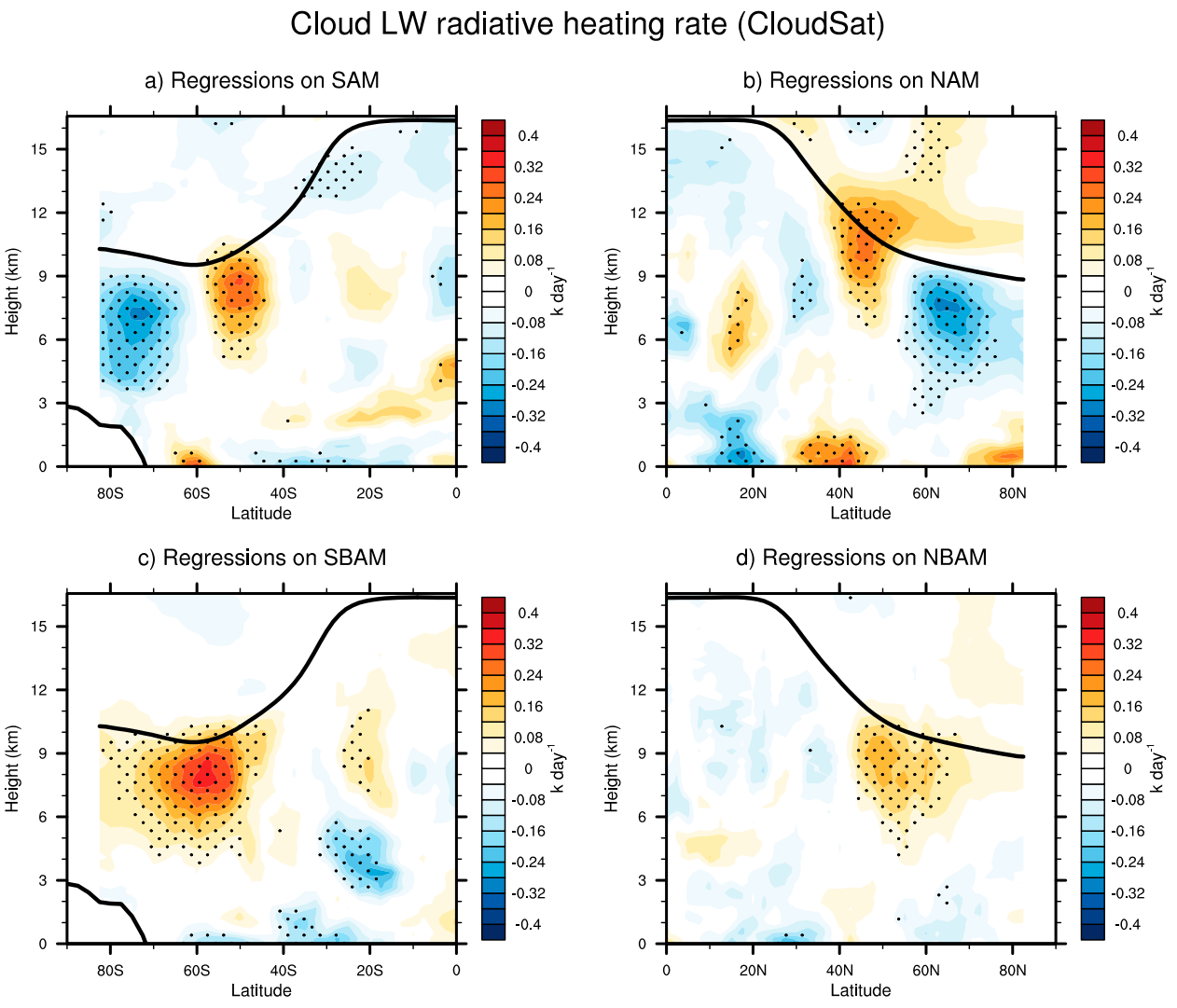

FIG. 5. (left) Regressions of pentad-mean, zonal mean cloud longwave radiative heating rates onto standardized pentad mean values of the (a) SAM, (b) NAM, (c) SBAM, and (d) NBAM indices. The cloud-induced radiative heating rates are defined as the differences between the all-sky and clear-sky radiative heating rates. The thick black line indicates the height of the climatological-mean tropopause and zonally averaged surface elevation over Antarctica. Black stippling indicates results that exceed the 95% confidence level based on a two-tailed test of the *t* statistic, with the effective degrees of freedom computed as per Bretherton et al. [1999, their Eq. (31)]. Cloud radiative heating rates are derived from the *CloudSat* 2B-FLXHR-lidar product. Results are based on the period January 2007–December 2010.

ACRE in the midlatitude troposphere where cloud incidence is anomalously low, and vice versa at subpolar latitudes. The baroclinic annular modes are dominated by positive ACRE anomalies above ~6 km between ~45° and 65° (Figs. 6c,d) where cloud incidence is anomalously high (Figs. 3c,d). However, note that the shortwave ACRE anomalies are as much as 40 times smaller than the associated changes in longwave ACRE (note the different color scales) and thus play a much smaller role in determining the total anomalies in ACRE.

2) SURFACE CLOUD RADIATIVE EFFECTS

Longwave cloud radiative effects are manifested primarily within the atmosphere and arise from the absorption and emission of longwave radiation by clouds. In contrast, shortwave cloud radiative effects are manifested primarily at the surface and arise primarily from the reflection of solar radiation by clouds (Allan 2011). Figure 7 shows the changes in daily-mean surface cloud radiative effects associated with annular mode variability based on CERES observations.

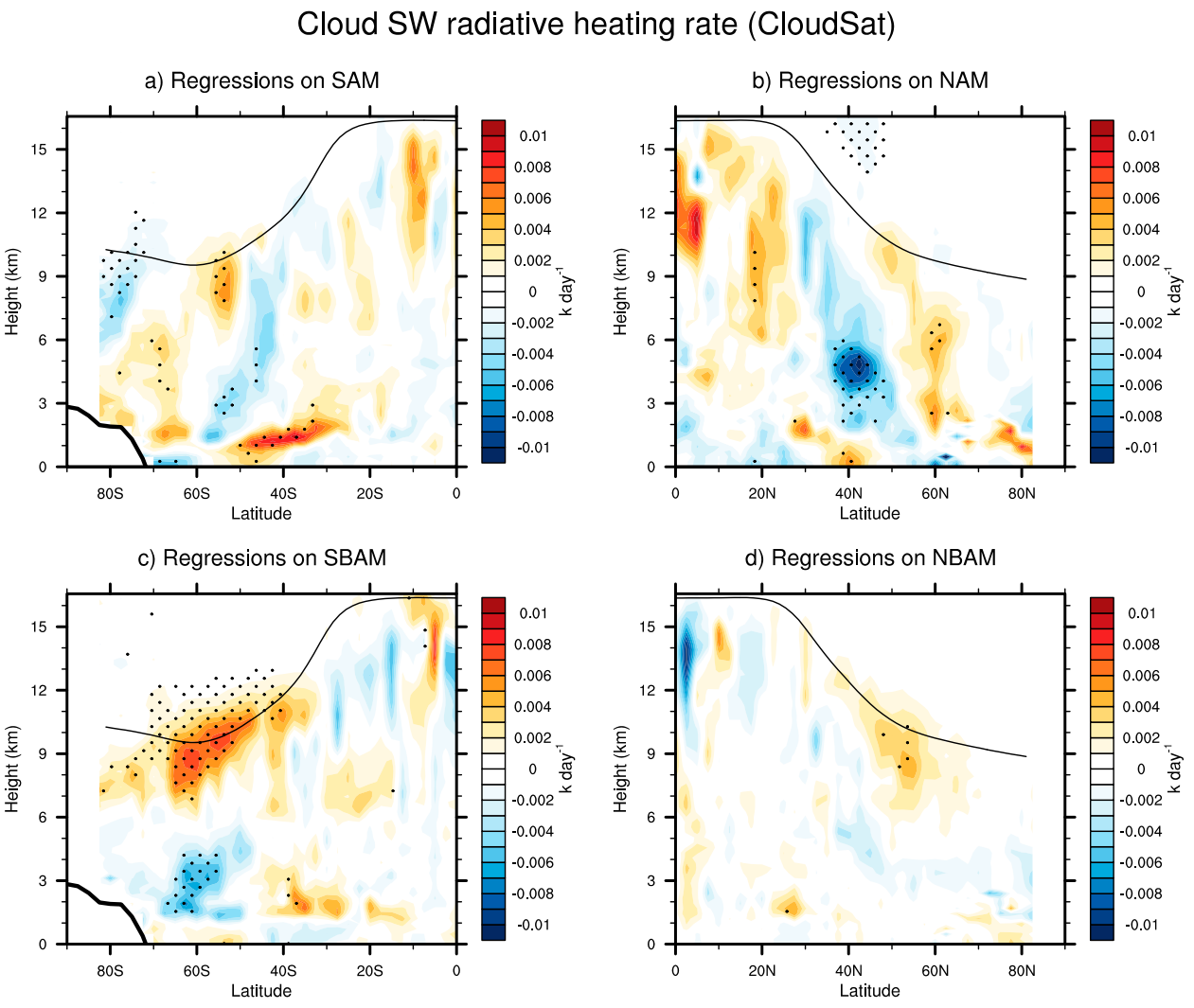

FIG. 6. As in Fig. 5, but for the shortwave radiating heating rates.

In the case of the SAM, the anomalous shortwave surface cloud radiative effects are dominated by decreases in shortwave absorption at ~40°S, which coincide closely with the increases in cloud incidence in the lowermost troposphere. Interestingly, the SAM is not associated with substantial changes in the surface shortwave radiative fluxes at latitudes poleward of about 50°S. This suggests that the complicated pattern of cloud incidence anomalies associated with the SAM (Fig. 1c) does not yield notable differences in the amount of solar radiation reaching the surface, perhaps because changes in shortwave surface cloud radiative effects are more dependent on the changes of cloud optical depth than total cloud amount at these latitudes (e.g., Zelinka et al. 2012; McCoy et al. 2014; Ceppi et al. 2016; Ceppi and Hartmann 2016).

In the case of the NAM, the anomalous shortwave surface cloud radiative effects are marked by increases in shortwave absorption at ~40°N, and decreases in shortwave absorption near 20° and 60°N. The meridional pattern of shortwave fluxes is very different from that associated with the SAM. Unlike the SAM, the NAM has a relatively weak signature in low-level clouds (Fig. 1d). Hence its signature in shortwave cloud radiative effects appears to derive mainly from the changes in the cloud incidence at the midtroposphere: the decreases in midtropospheric clouds near 40°N (Fig. 1d) overlie increases in shortwave surface radiative fluxes; the increases in midtropospheric clouds near 60°N (Fig. 1d) overlie decreases in shortwave surface radiative fluxes.

In the case of the SBAM and NBAM, the shortwave surface cloud radiative effects are generally negative between ~20° and 70° (Figs. 7c,d). The negative surface cloud radiative effects are consistent with increases in cloud incidence in most of the free troposphere (Figs. 3c,d).

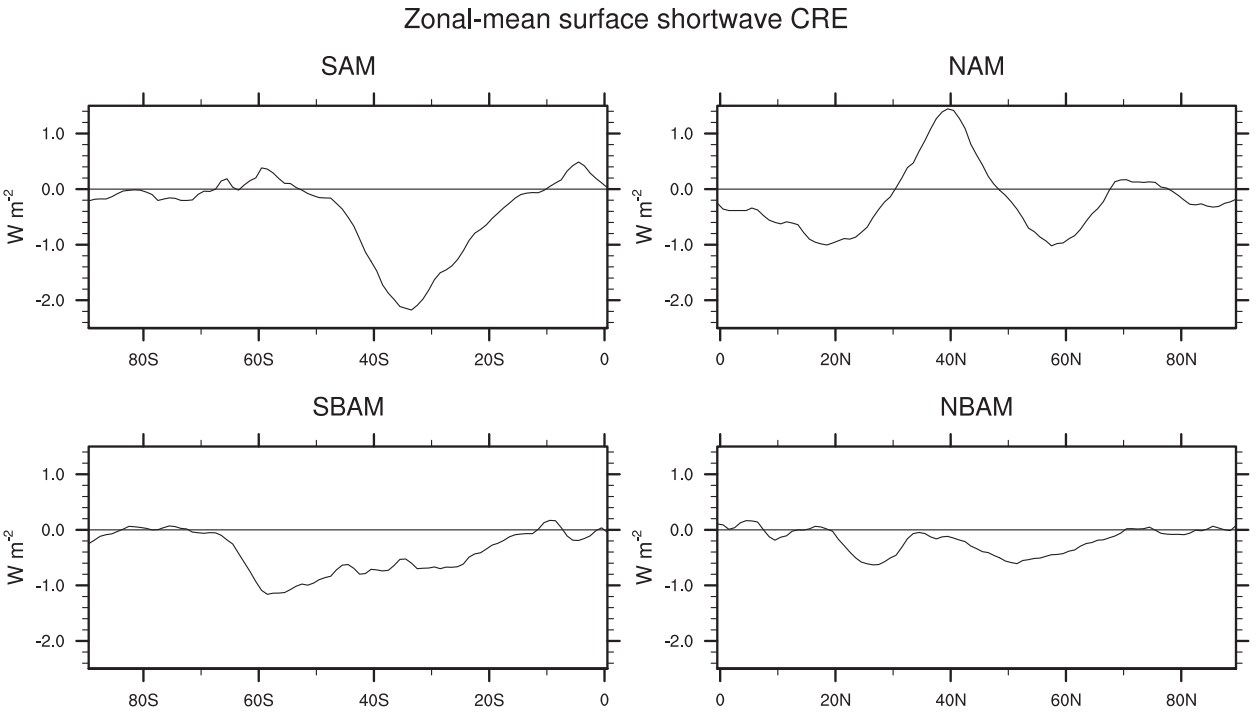

FIG. 7. Regressions of daily-mean, zonal mean cloud shortwave radiative effects at the surface onto standardized daily-mean values of the (a) SAM, (b) NAM, (c) SBAM, and (d) NBAM indices. The surface cloud radiative effects are defined as the differences between the all-sky and clear-sky surface radiative effects. Downward flux is defined as positive. Results are calculated based on daily-mean CERES observations (January 2001–December 2011).

d. Quasi-periodic behavior in the SBAM

The time series of the SBAM exhibits robust periodicity on time scales of ~20–30 days (Thompson and Woodworth 2014). The periodicity in the SBAM extends to hemispheric averages of eddy kinetic energy, eddy heat fluxes, and precipitation (Thompson and Barnes 2014). In Fig. 8, we examine to what extent it also extends to hemispherically averaged longwave cloud radiative effects.

Figure 8a show power spectra of outgoing longwave radiation (OLR) averaged over the SH midlatitudes (35°–75°S) from two different satellite data sources. Consistent with the spectral peak in the hemispheric averages of precipitation (Thompson and Barnes 2014), OLR integrated over the SH midlatitudes also exhibits periodic behavior on ~20–30-day time scales. Figure 8b show the corresponding power spectra of SH-mean TOA longwave cloud radiative effects. The spectral peak on ~20–30-day time scales in TOA longwave cloud radiative effects is clearly robust and reproducible in both data sources.

The NBAM is also associated with same-signed changes in TOA longwave cloud radiative effects throughout the extratropics. However, it exhibits only weak periodicity (Thompson and Li 2015), and the TOA longwave cloud radiative effects averaged over the NH do not exhibit a robust spectral peak on ~20–30-day time scales (not shown).

4. Summary and discussion

The purpose of this contribution is to analyze and interpret the signatures of the annular modes in the vertical structure of clouds and cloud radiative effects. The paper exploits a host of remotely sensed products including, importantly, *CloudSat* observations. The primary findings are the following:

1) The vertically varying signatures of the barotropic annular modes in cloud incidence have a complex vertical structure:
   - In the upper troposphere and lower stratosphere, the positive polarities of the NAM and SAM are characterized by negative anomalies in clouds at subpolar latitudes and positive anomalies at middle latitudes. The NAM has a weak additional center of action in the subtropics. The changes in upper tropospheric clouds are consistent with the attendant changes in upper tropospheric stability.
   - In the middle troposphere, the NAM and SAM are again characterized by a meridional dipole in cloud incidence between subpolar and middle latitudes,

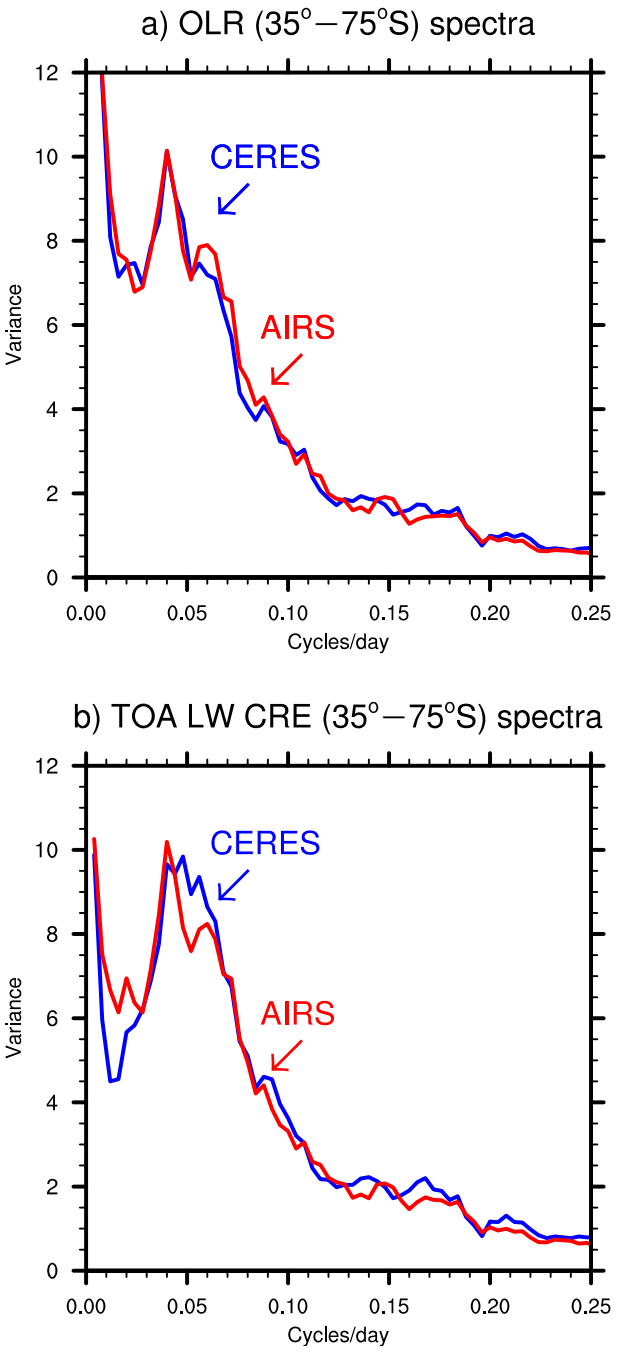

FIG. 8. (top) Power spectra of outgoing longwave radiation (OLR) and (bottom) TOA longwave cloud radiative effects (LW CRE) averaged over 35°–75°S. Results are calculated based on daily-mean AIRS observations (red; January 2000–December 2014) and CERES observations (blue; March 2000–November 2014).

but the anomalies are the opposite sign of those in the upper troposphere. The changes in middle tropospheric clouds are consistent with the anomalies in large-scale vertical motion.

- In the lowermost troposphere, the positive polarity of the SAM is characterized by positive anomalies in cloud incidence ~40° and negative anomalies ~60°. The changes in lower tropospheric clouds are consistent with the change in near-surface static stability and are only weakly apparent in association with the NAM.

2) The baroclinic annular modes have a much simpler vertical structure in cloud incidence. They are primarily associated with same-signed anomalies in cloud incidence extending throughout the troposphere at middle to high latitudes. The increases in mid- and high-level cloud incidence during the positive polarities of the SBAM and NBAM are consistent with the underlying changes in upward motion, static stability, and eddy amplitudes.
3) All of the annular modes are marked by changes in cloud radiative effects consistent with their signatures in cloud incidence. In general, the changes in atmospheric cloud radiative effects have largest amplitude in the upper troposphere and are dominated by the longwave component. Regions of increased upper-level cloud incidence are associated with enhanced longwave radiative warming, and vice versa. Changes in surface cloud radiative can be broadly interpreted in the context of the overlying changes in cloud incidence.
4) Southern Hemisphere mean longwave cloud radiative effects at the TOA exhibit a robust spectral peak on ~20–30-day time scales, consistent with the signature of the SBAM in cloud incidence.

The current study is part of a growing body of research that examines the coupling between large-scale dynamics and clouds at extratropical latitudes [e.g., see the review by Ceppi and Hartmann (2015), and references therein]. We have focused on patterns in cloud incidence and cloud radiative effects that are consistent with forcing by large-scale climate variability. We have not assessed cloud radiative feedbacks explicitly. But it is plausible that the changes in cloud radiative effects shown here could feed back onto the large-scale circulation through the changes in atmospheric and surface heating. Li et al. (2014a) speculate that the TOA cloud radiative effects associated with the NAM may act to shorten the time scale of its variations. Crueger and Stevens (2015) suggest that atmospheric cloud radiative effects influence the Madden–Julian oscillation. The results shown here indicate that the SBAM gives rise to periodic behavior in TOA longwave cloud radiative effects averaged over SH midlatitudes. They also indicate that the positive polarities of the SAM and NAM are associated with cloud radiative effects that act to enhance free tropospheric baroclinicity (through the anomalous longwave ACRE; see Figs. 5a,b),

but suppress surface baroclinicity (through the anomalous shortwave surface cloud radiative effects; Figs. 7a, b). The potential for two-way coupling between cloud radiative effects and the large-scale extratropical circulation will be explored in a future paper.

Acknowledgments. We thank Kevin Grise, Paulo Ceppi, and anonymous reviewers for their helpful comments. YL is funded by *CloudSat* via NASA JPL and the NSF Climate Dynamics program. DWJT is funded by the NSF Climate Dynamics program.

APPENDIX A

Comparing Cloud Vertical Structure Derived from *CloudSAT* data and ERA-Interim

Figure A1 compares results based on *CloudSat* data (left) and the ERA-Interim reanalysis for the *CloudSat* period (middle) and extended 1979–2011 period (right). The results are shown for two reasons: 1) to demonstrate the reproducibility of the cloud incidence anomalies based on *CloudSat* in ERA-Interim (cf. left and middle columns) and 2) to demonstrate the reproducibility of results based on the relatively short *CloudSat* era in those derived from a much longer period of record (cf. middle and right columns).

For the most part, the results based on *CloudSat* are very similar to those based on ERA-Interim. Thus these results can be used to validate model simulations of cloud–circulation interactions. The differences may arise from several factors. The reanalysis cloud fraction data are based on model parameterizations of cloud processes; the *CloudSat*/*CALIPSO* data are derived from a spaceborne radar and lidar. The reanalysis cloud fraction data include full spatial coverage, have relatively long temporal sampling, and are consistent with changes in large-scale dynamics. The *CloudSat* data have limited spatial (along-track) and temporal (June 2006–April 2011) sampling. A quantitative comparison of the results based on *CloudSat*/*CALIPSO* and ERA-Interim would require applying a *CloudSat*/*CALIPSO* simulator to the ERA-Interim output. But such a detailed treatment of the differences is beyond the scope of this study.

APPENDIX B

Horizontal Structures of the Cloud Incidence Associated with Annular Variability

Figure B1 shows the horizontal structures of cloud incidence anomalies vertically averaged over indicated levels (chosen on the basis of the amplitude of the zonal-mean signal).

The signatures of the annular modes in cloud incidence are more zonally symmetric in the Southern Hemisphere than those in the Northern Hemisphere. In the case of the NAM, strong zonal asymmetry is notable over the North American/North Atlantic sector, and the amplitude of the meridional triple is pronounced over the North Atlantic sector (Fig. B1b). In the case of the NBAM (Fig. B1f), the positive anomalies in cloud incidence peak upstream of the North Pacific and Atlantic storm tracks, and are primarily over the regions with enhanced local eddy kinetic energy [also see Fig. 6 in Thompson and Li (2015)].

APPENDIX C

The Robustness of the Structure of the NAM in Cloud Incidence to Changes in Analysis Design

The cloud incidence anomalies in Figs. 1d and 2d reveal a meridional tripole in upper tropospheric clouds associated with the NAM that is not apparent in our previous analyses (Li et al. 2014a). As noted in the main text, the differences in the signature of the NAM in upper tropospheric cloud structure shown in this study and in Li et al. (2014a) arise from several differences in analysis technique. The effects of these differences are documented in Fig. C1. Results in the left column are based on the leading PC of the zonal-mean wind at all tropospheric levels (as used in this study); results in the right column are based on the leading PC of height at 1000 hPa [as used in Li et al. (2014a)]. Results in the top row are based on pentad-mean data (as used in this study), in the middle row on monthly-mean data for all calendar months, and in the bottom on monthly-mean data for the winter months only [as used in Li et al. (2014a)]. Note that results in Fig. C1a are reproduced from Fig. 1d, and results in Fig. C1f are reproduced from our previous analysis [cf. Fig. 1c in Li et al. (2014a)]. In general, the meridional tripole in upper tropospheric clouds has larger amplitude in regressions based on pentad-mean data relative to monthly-mean data (pentad data afford a larger sample size and include submonthly variations, and thus the relationships between clouds and the meteorology are expected to be more robust in analyses based on synoptic rather than monthly time scales), and in regressions based on the leading PC of zonal-mean zonal wind relative to the leading PC of height at 1000 hPa (the former index is calculated using data from all tropospheric levels, and is thus expected to better capture variations in the NAM in the upper troposphere).

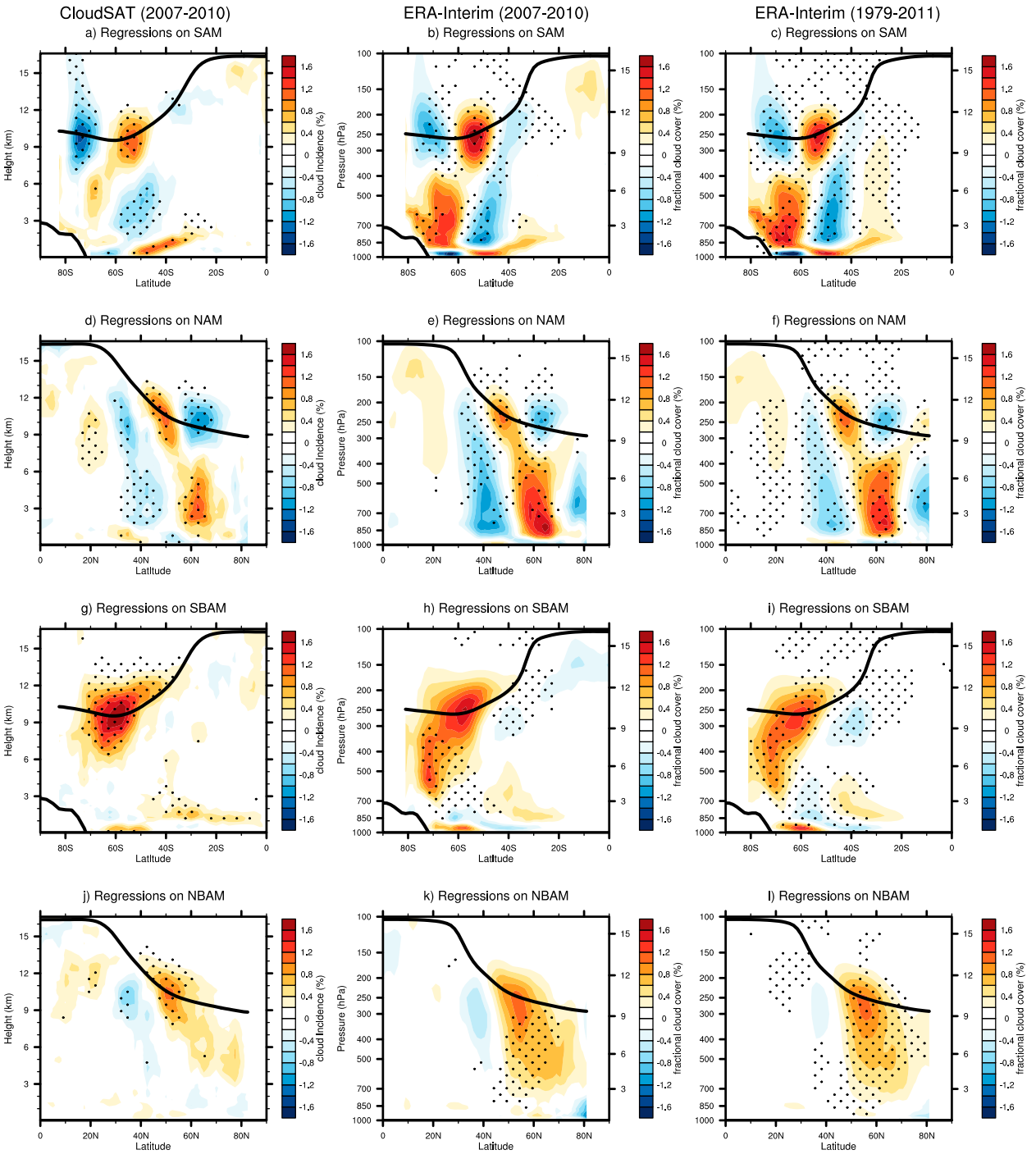

FIG. A1. Comparing the cloud vertical structures associated with the four annular modes in *CloudSat* observations and ERA-Interim reanalysis. Results in the left panels are reproduced from the shading in the bottom panels of Figs. 1 and 3. Results in the middle and right panels show the corresponding regressions based on daily-mean, zonal-mean cloud fractional cover from ERA-Interim based on the period 2007–10 and 1979–2011, respectively. ERA-Interim results are masked out poleward of 82° (the latitudinal limit of the *CloudSat* data). The thick black line indicates the height of the climatological-mean tropopause and zonally averaged surface elevation over Antarctica. Black stippling indicates results that exceed the 95% confidence level based on a two-tailed test of the t statistic, with the effective degrees of freedom computed as per Bretherton et al. [1999, their Eq. (31)].

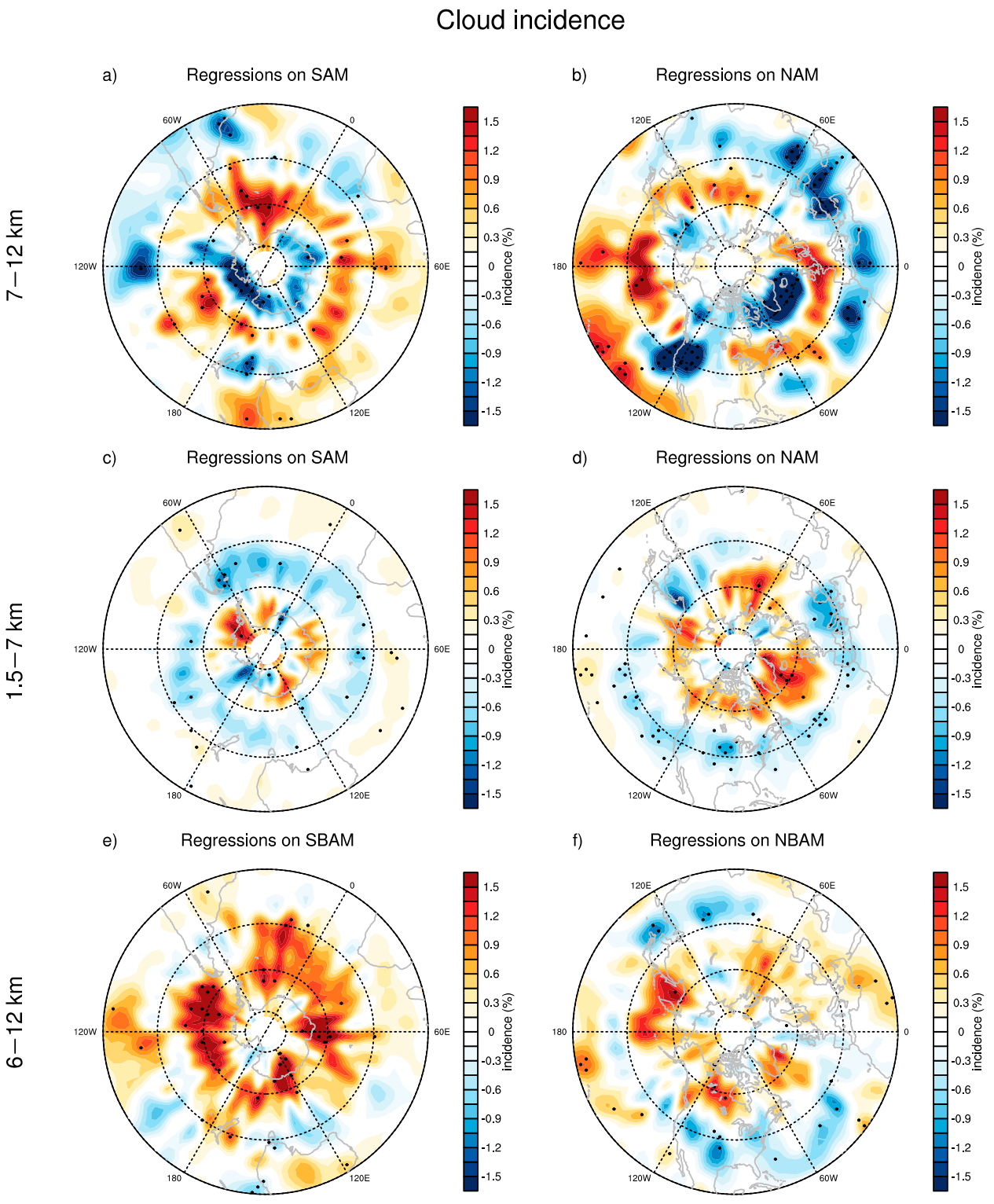

FIG. B1. Horizontal distribution of the regressions of pentad-mean cloud incidence (top) averaged between 7 and 12 km for the SAM and NAM, (middle) averaged between 1.5 and 7 km for the SAM and NAM, and (bottom) averaged between 6 and 12 km for the SBAM and NABAM. Black stippling indicates results that exceed the 95% confidence level based on a two-tailed test of the t statistic, with the effective degrees of freedom computed as per Bretherton et al. [1999, their Eq. (31)]. The results have been smoothed with an NCAR Command Language built-in 9-point smoothing function for the purpose of display only.

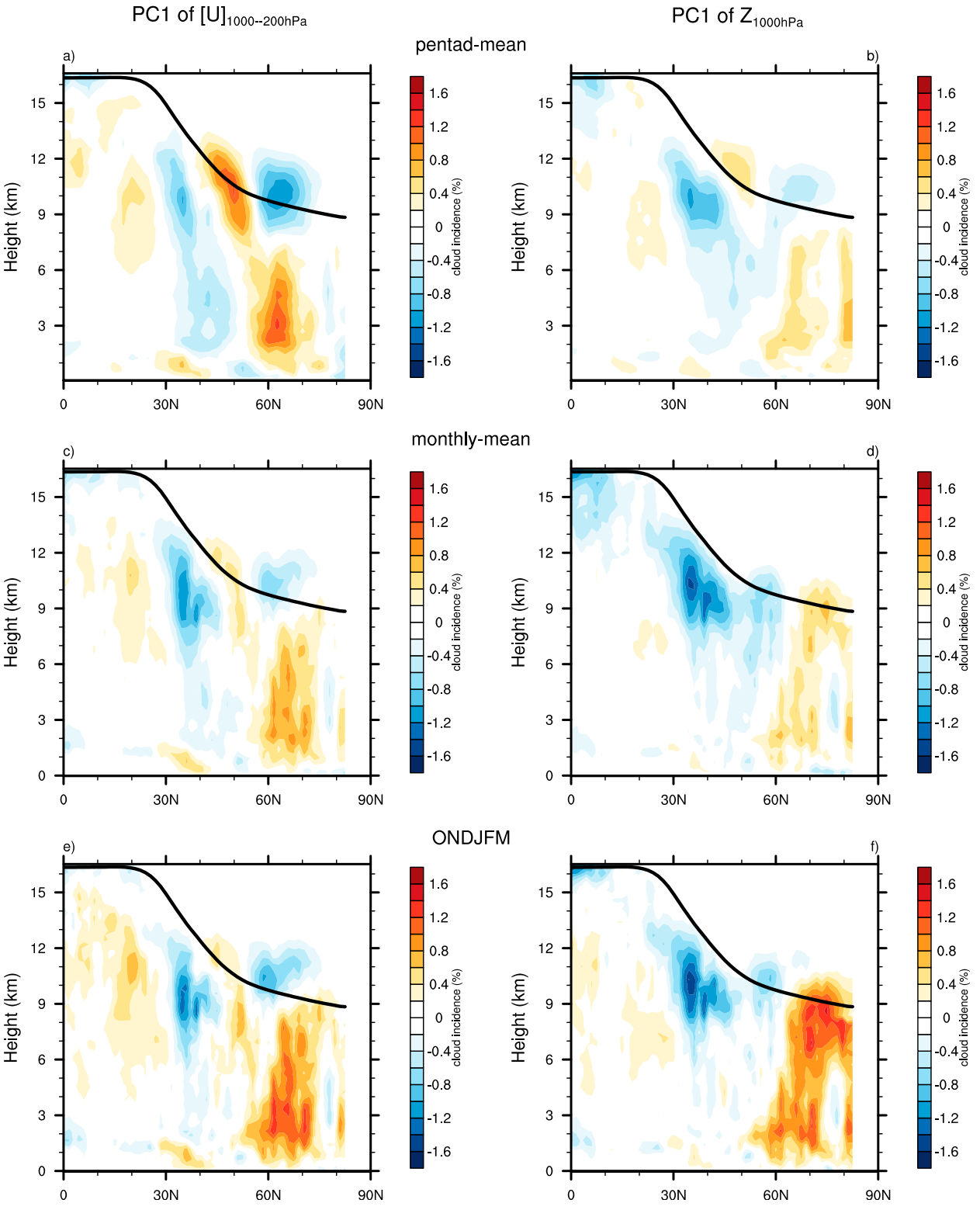

FIG. C1. Comparison of (left) the cloud vertical structures associated with the leading PC time series of the zonal-mean zonal wind used in this study (the PC is calculated over all levels and latitudes within the domain 1000–200 hPa and 20°–70°N) and (right) the leading PC of height at 1000 hPa used in Li et al. (2014a). Results are based on (a),(b) pentad-mean data, (c),(d) monthly-mean data for all calendar months, and (e),(f) monthly-mean data for the wintertime months (bottom). Results in (a) are reproduced from Fig. 1d, and results in (f) are reproduced from Fig. 1c in Li et al. (2014a).

REFERENCES

Allan, R. P., 2011: Combining satellite data and models to estimate cloud radiative effect at the surface and in the atmosphere. *Meteor. Appl.*, **18**, 324–333, doi:10.1002/met.285.

Aumann, H. H., and Coauthors, 2003: AIRS/AMSU/HSB on the Aqua mission: Design, science objectives, data products, and processing systems. *IEEE Trans. Geosci. Remote Sens.*, **41**, 253–264, doi:10.1109/TGRS.2002.808356.

Bretherton, C. S., M. Widmann, V. P. Dymnikov, J. M. Wallace, and I. Bladé, 1999: The effective number of spatial degrees of freedom of a time-varying field. *J. Climate*, **12**, 1990–2009, doi:10.1175/1520-0442(1999)012<1990:TENOSD>2.0.CO;2.

Ceppi, P., and D. L. Hartmann, 2015: Connections between clouds, radiation, and midlatitude dynamics: A review. *Curr. Climate Change Rep.*, **1**, 94–102, doi:10.1007/s40641-015-0010-x.

——, and ——, 2016: Clouds and the atmospheric circulation response to warming. *J. Climate*, **29**, 783–799, doi:10.1175/JCLI-D-15-0394.1.

——, M. D. Zelinka, and D. L. Hartmann, 2014: The response of the Southern Hemispheric eddy-driven jet to future changes in shortwave radiation in CMIP5. *Geophys. Res. Lett.*, **41**, 3244–3250, doi:10.1002/2014GL060043.

——, D. Hartmann, and M. Webb, 2016: Mechanisms of the negative shortwave cloud feedback in mid to high latitudes. *J. Climate*, **29**, 139–157, doi:10.1175/JCLI-D-15-0327.1.

Chahine, M., and Coauthors, 2006: AIRS: Improving weather forecasting and providing new data on greenhouse gases. *Bull. Amer. Meteor. Soc.*, **87**, 911–926, doi:10.1175/BAMS-87-7-911.

Crueger, T., and B. Stevens, 2015: The effect of atmospheric radiative heating by clouds on the Madden–Julian oscillation. *J. Adv. Model. Earth Syst.*, **7**, 854–864, doi:10.1002/2015MS000434.

Dee, D. P., and Coauthors, 2011: The ERA-Interim reanalysis: Configuration and performance of the data assimilation system. *Quart. J. Roy. Meteor. Soc.*, **137**, 553–597, doi:10.1002/qj.828.

Grise, K. M., and L. M. Polvani, 2014: Southern Hemisphere cloud dynamics biases in CMIP5 models and their implications for climate projections. *J. Climate*, **27**, 6074–6092, doi:10.1175/JCLI-D-14-00113.1.

——, ——, G. Tselioudis, Y. Wu, and M. D. Zelinka, 2013: The ozone hole indirect effect: Cloud-radiative anomalies accompanying the poleward shift of the eddy-driven jet in the Southern Hemisphere. *Geophys. Res. Lett.*, **40**, 3688–3692, doi:10.1002/grl.50675.

Hartmann, D., and F. Lo, 1998: Wave-driven zonal flow vacillation in the Southern Hemisphere. *J. Atmos. Sci.*, **55**, 1303–1315, doi:10.1175/1520-0469(1998)055<1303:WDZFVI>2.0.CO;2.

Haynes, J. M., T. H. V. Haar, T. L'Ecuyer, and D. Henderson, 2013: Radiative heating characteristics of Earth's cloudy atmosphere from vertically resolved active sensors. *Geophys. Res. Lett.*, **40**, 624–630, doi:10.1002/grl.50145.

Henderson, D. S., T. L'Ecuyer, G. Stephens, P. Partain, and M. Sekiguchi, 2013: A multisensor perspective on the radiative impacts of clouds and aerosols. *J. Appl. Meteor. Climatol.*, **52**, 853–871, doi:10.1175/JAMC-D-12-025.1.

Kato, S., N. G. Loeb, F. G. Rose, D. R. Doelling, D. A. Rutan, T. E. Caldwell, L. Yu, and R. A. Weller, 2013: Surface irradiances consistent with CERES-derived top-of-atmosphere shortwave and longwave irradiances. *J. Climate*, **26**, 2719–2740, doi:10.1175/JCLI-D-12-00436.1.

Klein, S. A., and D. L. Hartmann, 1993: The seasonal cycle of low stratiform clouds. *J. Climate*, **6**, 1587–1606, doi:10.1175/1520-0442(1993)006<1587:TSCOLS>2.0.CO;2.

Li, Y., D. W. J. Thompson, Y. Huang, and M. Zhang, 2014a: Observed linkages between the northern annular mode/North Atlantic Oscillation, cloud incidence, and cloud radiative forcing. *Geophys. Res. Lett.*, **41**, 1681–1688, doi:10.1002/2013GL059113.

——, ——, G. L. Stephens, and S. Bony, 2014b: A global survey of the instantaneous linkages between cloud vertical structure and large-scale climate. *J. Geophys. Res. Atmos.*, **119**, 3770–3792, doi:10.1002/2013JD020669.

Limpasuvan, V., and D. L. Hartmann, 2000: Wave-maintained annular modes of climate variability. *J. Climate*, **13**, 4414–4429, doi:10.1175/1520-0442(2000)013<4414:WMAMOC>2.0.CO;2.

Loeb, N. G., B. A. Wielicki, D. R. Doelling, G. L. Smith, D. F. Keyes, S. Kato, N. Manlo-Smith, and T. Wong, 2009: Toward optimal closure of the Earth's top-of-atmosphere radiation budget. *J. Climate*, **22**, 748–766, doi:10.1175/2008JCLI2637.1.

Mace, G. G., Q. Zhang, M. Vaughn, R. Marchand, G. Stephens, C. Trepte, and D. Winker, 2009: A description of hydrometeor layer occurrence statistics derived from the first year of merged CloudSat and CALIPSO data. *J. Geophys. Res.*, **114**, D00A26, doi:10.1029/2007JD009755.

——, S. Houser, S. Benson, S. A. Klein, and Q. Min, 2011: Critical evaluation of the ISCCP simulator using ground-based remote sensing data. *J. Climate*, **24**, 1598–1612, doi:10.1175/2010JCLI3517.1.

McCoy, D. T., D. L. Hartmann, and D. P. Grosvenor, 2014: Observed Southern Ocean cloud properties and shortwave reflection. Part II: Phase changes and low cloud feedback. *J. Climate*, **27**, 8858–8868, doi:10.1175/JCLI-D-14-00288.1.

Simmons, A., S. Uppala, D. Dee, and S. Kobayashi, 2007: ERA-Interim: New ECMWF reanalysis products from 1989 onwards. ECMWF Newsletter, No. 110, ECMWF, Reading, United Kingdom, 25–35.

Thompson, D. W. J., and J. M. Wallace, 2000: Annular modes in the extratropical circulation. Part I: Month-to-month variability. *J. Climate*, **13**, 1000–1016, doi:10.1175/1520-0442(2000)013<1000:AMITEC>2.0.CO;2.

——, and E. A. Barnes, 2014: Periodic variability in the large-scale Southern Hemisphere atmospheric circulation. *Science*, **343**, 641–645, doi:10.1126/science.1247660.

——, and J. D. Woodworth, 2014: Barotropic and baroclinic annular variability in the Southern Hemisphere. *J. Atmos. Sci.*, **71**, 1480–1493, doi:10.1175/JAS-D-13-0185.1.

——, and Y. Li, 2015: Baroclinic and barotropic annular variability in the Northern Hemisphere. *J. Atmos. Sci.*, **72**, 1117–1136, doi:10.1175/JAS-D-14-0104.1.

Zelinka, M., S. Klein, and D. Hartmann, 2012: Computing and partitioning clouds feedbacks using cloud property histograms. Part II: Attribution to changes in cloud amount, altitude, and optical depth. *J. Climate*, **25**, 3736–3754, doi:10.1175/JCLI-D-11-00249.1.